CHINESE OPTICS LETTERS

Vol. 21, No. 4 | April 2023

Satellite-to-aircraft quantum key distribution performance estimation with boundary layer effects

Huicun Yu (于惠存)[1,2], Bangying Tang (唐帮盈)[3], Jiahao Li (李佳豪)[1], Yuexiang Cao (曹跃翔)[1], Han Zhou (周 涵)[3], Sichen Li (李斯晨)[3], Haoxi Xiong (熊浩西)[4], Bo Liu (刘 博)[2*], and Lei Shi (石 磊)[1**]

[1] Information and Navigation College, Air Force Engineering University, Xi'an 710077, China

[2] College of Advanced Interdisciplinary Studies, National University of Defense Technology, Changsha 410073, China

[3] College of Computer and Science, National University of Defense Technology, Changsha 410073, China

[4] Teaching and Research Support Center, National University of Defense Technology, Changsha 410073, China

*Corresponding author: liubo08@nudt.edu.cn

**Corresponding author: slfly2012@163.com

Received September 27, 2022 | Accepted December 6, 2022 | Posted Online March 24, 2023

Remarkable progress has been made in satellite-based quantum key distribution (QKD), which can effectively provide QKD service even at the intercontinental scale and construct an ultralong-distance global quantum network. But there are still some places where terrestrial fiber and ground stations cannot be constructed, like harsh mountainous areas and air space above the sea. So the airborne platform is expected to replace the ground station and provide flexible and relay links for the large-scale integrated communication network. However, the photon transmission rate would be randomly reduced, owing to the randomly distributed boundary layer that surrounds the surface of the aircraft when the flight speed is larger than 0.3 Ma. Previous research of airborne QKD with boundary layer effects is mainly under the air-to-ground scenario in which the aircraft is a transmitter, while the satellite-to-aircraft scenario is rarely reported. In this article, we propose a performance evaluation scheme of satellite-to-aircraft QKD with boundary layer effects in which the aircraft is the receiver. With common experimental settings, the boundary layer would introduce a ∼31 dB loss to the transmitted photons, decrease ∼47% of the quantum communication time, and decrease ∼51% of the secure key rate, which shows that the aero-optical effects caused by the boundary layer cannot be ignored. Our study can be performed in future airborne quantum communication designs.

Keywords: satellite-to-aircraft quantum key distribution; boundary layer; aero-optical effects.

DOI: 10.3788/COL202321.042702

1. Introduction

Based on quantum mechanics, quantum key distribution (QKD) can realize security key sharing between remote communication parties, which plays an important role in our modern information society[1–5]. In order to build the integrated quantum communication network, substantial progress has been achieved in both theoretical and experimental aspects, especially those that are fiber-based[6–9] and satellite-based[10–16] QKD. In 2021, the world's first large-scale quantum communication network was constructed that integrated more than 700 terrestrial optical fiber QKD links and two high-speed QKD links in satellite-terrestrial free space, which enabled any user in the network to communicate in a distance of 4600 km[16]. It shows that the quantum satellites can effectively provide QKD service even at the intercontinental scale and construct ultralong-distance global quantum networks. However, there are still some places where terrestrial fiber and ground stations cannot be constructed, like harsh mountainous areas, and air space above the sea. So airborne quantum nodes are expected to replace ground stations and provide flexible and relay links for large-scale integrated communication networks[17]. Compared with satellite-to-station QKD, satellite-to-aircraft QKD features low atmospheric loss and long transmission distance, owing to the photon loss and turbulence predominantly occurring in the lower ∼10 km of the atmosphere[18].

Since the first aircraft-based QKD experiment was verified successfully in 2013[19], in the past decade, numerous studies have been focusing on the challenges of airborne QKD links[19–25]. Compared with ground stations, airborne QKDs feature high-speed maneuverability and suffer complicated atmosphere conditions that include atmospheric turbulence[26–30], background noise[31–33], and attitude disturbance[14]. Furthermore, a very thin layer of air will stick over

the surface of the aircraft with high velocity, resulting in the boundary layer (BL)[34,35]. It has been proved that the BL effect will seriously affect the airborne QKD performance when the aircraft speed is higher than 0.3 Ma[36]. However, previous research of airborne QKD with BL effects is mainly under the air-to-ground scenario, while the satellite-to-aircraft scenario, which is one of the essential components in constructing a globe-wide quantum-secure communication network, has rarely been reported.

In this article, we propose a performance evaluation scheme of satellite-to-aircraft QKD with BL effects. We first propose a satellite-to-aircraft QKD scenario with decoy BB84 protocol. Then, the wavefront aberration of quantum signal states is evaluated by estimating the reflection index distribution of the surrounded BL and performing the ray tracing method by the Adams linear multistep method, which starts with the satellite ephemeris and aircraft trajectory. Afterward, the photon transmission efficiency caused by wavefront aberration is evaluated by the Strehl ratio. Finally, the overall photon quantum bit error rate (QBER) and final secure key rate can be estimated. The analyzed photon transmission loss in different incident angles shows that the effects of the BL are more serious when the aircraft moves towards the satellite. With common experimental settings, the BL would introduce a 31 dB loss to the transmitted photons, decrease ~47% of the quantum communication time, and decrease ~51% of the secure key rate. Our detailed satellite-to-aircraft QKD performance evaluation study can be performed on future airborne quantum communication designs.

2. Preliminaries

2.1. Reference system conversions

The coordinates of satellite and aircraft in the WGS-84 coordinate system can be obtained from the satellite ephemeris and aircraft trajectory, as shown in Fig. 1. The points P and P' are the conventional terrestrial pole, the blue curve is the Greenwich meridian, r is the mean radius of the Earth, l_A is the longitude of the satellite in degrees, L_A is the latitude of the satellite in degrees, h_A is the satellite altitude, l_B is the longitude of aircraft in degrees, L_B is the latitude of aircraft in degrees, h_B is aircraft altitude, and γ is the angle between OA and OB.

In the ray-tracing methods, the satellite azimuth angle, the satellite elevation angle, and the distance between the satellite and aircraft are taken as the input parameters. Therefore, it is necessary to transform the WGS-84 coordinate system into the spherical coordinate system based on the aircraft, as shown in Fig. 2. The spherical coordinate system is established with the origin at the geometric center of the airborne receiver telescope. The x axis is parallel to the tangent direction of the longitude and points north. The y axis is parallel to the tangent direction of the longitude and points east. The z axis merges with the local vertical and points to the zenith. The positions of satellite and aircraft in the coordinate system are S and O. The azimuth angle α, the elevation angle β, and the distance d between satellite and aircraft can be calculated by the following formula:

$$\alpha = \arctan\left[\frac{\sin(|l_A - l_B|)\cos(L_A)}{\cos(L_B)\sin(L_A) - \cos(L_A)\sin(L_B)\cos(L_B - L_A)}\right], \tag{1}$$

$$d = (r + h_A)\left[1 + \left(\frac{r + h_B}{r + h_A}\right)^2 - 2\left(\frac{r + h_B}{r + h_A}\right)\cos(\gamma)\right]^{1/2}, \tag{2}$$

$$\cos(\gamma) = \cos(L_B)\cos(L_A)\cos(l_A - l_B) + \sin(L_B)\sin(L_A), \tag{3}$$

$$\beta = \arccos\left[\frac{(r + h_A)\sin(\gamma)}{d}\right]. \tag{4}$$

2.2. Principle of ray-tracing methods

The aero-optical effects are fundamentally caused by the gradient refractive index n due to the variable-density flow field, which is expressed by the Gladstone–Dale equation[37],

$$n = 1 + \rho K_{\mathrm{GD}}, \tag{5}$$

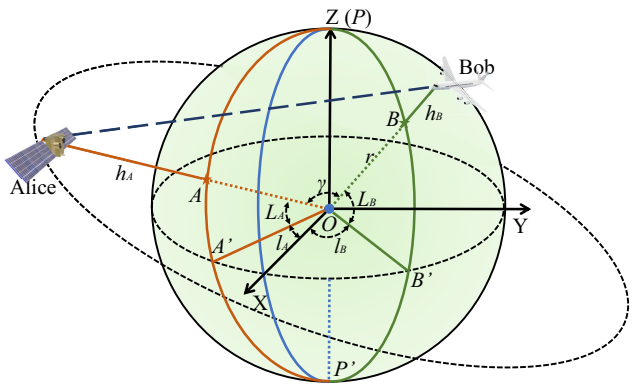

Fig. 1. Schematic diagram of satellite and aircraft in the WGS-84 coordinate system.

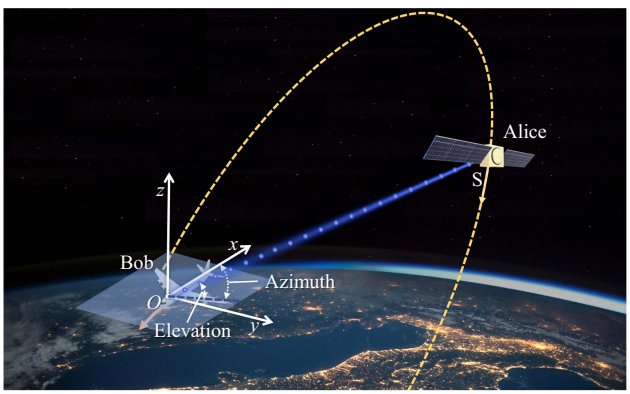

Fig. 2. Schematic diagram of downlink satellite-to-aircraft QKD in the spherical coordinate system based on the aircraft. The satellite (Alice) flies in a certain orbit above the receiving aircraft (Bob).

where ρ is the density of the flow field. K_{GD} is the Gladstone–Dale constant decided only by the wavelength λ (μm) of photons[37],

$$K_{GD} = 2.23 \times 10^{-4} \times \left(1 + \frac{7.52 \times 10^3}{\lambda^2}\right). \tag{6}$$

The trajectory of a ray in inhomogeneous media is determined by solving the ray equation[38],

$$\frac{\mathrm{d}}{\mathrm{d}p}\left(n\frac{\mathrm{d}s}{\mathrm{d}p}\right) = \nabla n, \tag{7}$$

where s is the position vector of a typical point on the ray, p is the path length of the ray, and ∇n is the gradient of the refractive index. Equation (7) can be written as a set of first-order differential equations,

$$\begin{cases} \frac{\mathrm{d}F}{\mathrm{d}p} = \nabla n \\ \frac{\mathrm{d}s}{\mathrm{d}p} = \frac{1}{n}F \end{cases}, \tag{8}$$

where F is the vector of light. The vectors s and F can be written as

$$s = \begin{pmatrix} x \\ y \\ z \end{pmatrix}, \qquad F = \begin{pmatrix} F_x \\ F_y \\ F_z \end{pmatrix} = n\begin{pmatrix} \frac{\mathrm{d}x}{\mathrm{d}p} \\ \frac{\mathrm{d}y}{\mathrm{d}p} \\ \frac{\mathrm{d}z}{\mathrm{d}p} \end{pmatrix}. \tag{9}$$

The ray path can be calculated by numerical solution[39,40].

2.3. Aero-optical effects

In the airborne QKD procedure, the BL effect is also called the aero-optical effect in classical optics. Aero-optical effects will be introduced to the photons, which are propagated through the density-varying flow field of the BL. Typical aero-optical effects mainly include wavefront aberration, jitter, intensity attenuation, and so on. Relevant parameters of aero-optical effects are the optical path length (OPL), the optical path difference (OPD), and the Strehl ratio (SR)[41].

The refractive index field of the airborne BL can be calculated by dividing the density field ρ into sufficiently small squares and performing the Gladstone–Dale equation. The scattered photon path P through the BL can be calculated by performing the ray-tracing methods.

The OPL of the photons is calculated by integrating the refractive index n along the propagation path P[42,43],

$$\mathrm{OPL}(x, y, t) = \int_P n(x, y, t)\mathrm{d}p. \tag{10}$$

OPD shows the configuration of the wavefront and is defined as

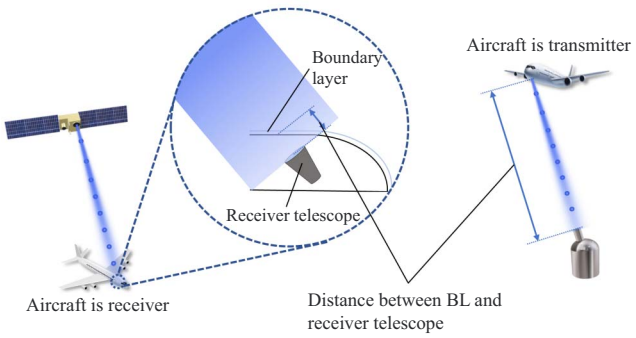

Fig. 3. Schematic diagram of the distance between the BL and receiver telescope.

$$\mathrm{OPD}(x, y, t) = \mathrm{OPL}(x, y, t) - \overline{\mathrm{OPL}}. \tag{11}$$

The overline denotes the spatial average over the optical aperture. The phase difference of the photons can be defined by

$$\phi = \frac{2\pi \cdot \mathrm{OPD}}{\lambda}. \tag{12}$$

There is a distance between the BL and receiver telescope, as shown in Fig. 3, which depends on whether the aircraft is a transmitter or receiver in the airborne QKD scenario. When the transmission distance is similar to the communication distance, all aero-optical effects introduced by the BL need to be considered. However, when the distance is far less than communication distance, even if the effect of the BL is introduced into the divergence angle and the deflection angle, the deflection and divergent effect could be ignored, but the wavefront aberration should be taken into consideration. As the distance is far less than communication distance in the satellite-to-aircraft downlink QKD scenario, only the wavefront aberration would have been taken into consideration.

3. Satellite-to-Aircraft QKD with BL Effects

Previous research on airborne QKD with BL effects is mainly under the air-to-ground scenario, with the aircraft as the transmitter and the ground station as the receiver. In this paper, the satellite is the transmitter and the aircraft is the receiver. The primary difference is that the distance between the BL and the receiving telescope is long in the air-to-ground scenario, whereas the distance is tight in the satellite-to-aircraft scenario. As mentioned in Section 2.3, due to the different distance, the performance evaluation schemes are different in the two scenarios. The performance evaluation procedure for satellite-to-aircraft QKD scheme is shown in Fig. 4.

3.1. Satellite-to-aircraft downlink QKD scenario

The satellite-to-aircraft downlink QKD scenario is shown in Fig. 2, the quantum photon source is located at the satellite (Alice), and the QKD receiving module with a spatial

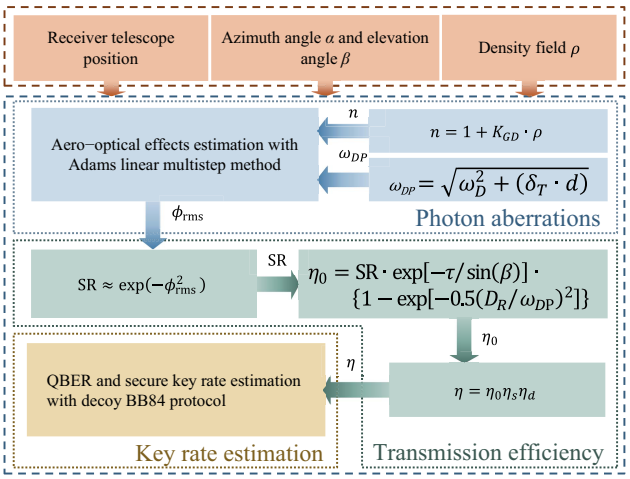

Fig. 4. Diagram of the satellite-to-aircraft QKD performance evaluation.

single-mode receiver is fixed in the upper fuselage of the aircraft (Bob). The receiver telescope position is temporarily set in a reasonable range. Assume that Alice is flying with a constant velocity, direction, and altitude. Given the aircraft specification, speed v, flying altitude h_B, and air density ρ_h, the density field distribution of the BL can be simulated by computational fluid dynamics software (such as CFX, Fluent, Star-CD, and COMSOL).

According to Section 2.1, the time-varying data of azimuth angle α ($0^\circ \le \alpha < 360^\circ$), the elevation angle β ($0^\circ \le \beta \le 90^\circ$), and the distance d between satellite and aircraft can be calculated by the satellite ephemeris and aircraft trajectory. Generally, the interval of $0^\circ \le \beta < 10^\circ$ is used for links calibration.

3.2. Satellite-to-aircraft QKD performance evaluation

The performance evaluation procedure for satellite-to-aircraft QKD scheme mainly contains three steps: photon aberrations evaluation, transmission efficiency calculation, and key rate estimation, as shown in Fig. 4.

3.2.1. Photon aberration

According to the downlink satellite-to-aircraft QKD scenario, the distance between the BL and the receiving telescope is tiny. The deflection and divergent effect from aero-optics can be ignored, and the effective beam waist of the downlink photon at the receiving telescope is constant, no matter whether the BL exists or not.

When the Gaussian mode beam is propagating through the BL to the aircraft, the effective beam waist ω_{DP} of the downlink photon at the receiving telescope can be expressed as

$$\omega_{\mathrm{DP}} = \sqrt{\omega_D^2 + (\sigma_T \cdot d)^2}, \tag{13}$$

where σ_T is the pointing error of the transmitter telescope.

ω_D is the beam waist at the ground station prior to pointing errors,

$$\omega_D = d\frac{\lambda}{\pi \cdot \omega_0}\left[1 + \frac{0.83}{\sin\beta}\left(\frac{D_T}{r_0}\right)^{5/3}\right]^{3/5}, \tag{14}$$

where r_0 is the Fried parameter in zenith[44], and D_T is the diameter of the transmitter telescope. $\omega_0 = 0.316D_T$ is the waist radius of the transmitted Gaussian beam[44].

According to Section 2.1, we establish the spherical coordinate system with the origin at the geometric center of the airborne receiver telescope, as shown in Fig. 5. We take sufficient incident points uniformly in the light spot range with the radius of the effective beam waist ω_{DP}, and the initial value of s in Section 2.2 can be denoted as

$$s_0 = \begin{bmatrix} x_1 & y_1 & z_1 \\ x_2 & y_2 & z_2 \\ \vdots & \vdots & \vdots \\ x_m & y_m & z_m \end{bmatrix}, \tag{15}$$

where m is the number of incident points. The initial value of F can be denoted as

$$F_0 = n\begin{pmatrix} \cos\alpha\cos\beta \\ \sin\alpha\cos\beta \\ \sin\beta \end{pmatrix}, \tag{16}$$

where n is the refractive index field of the BL, which can be calculated by the density field distribution in Eq. (5). And, using fourth-order Runge–Kutta method, Eq. (8) can be expanded as

$$\begin{cases} r_{n+1} = r_n + \frac{1}{6}h\left\{T_n + 2\left[T_n + \frac{h}{2}D(r_n)\right] + 2\left[T_n + \frac{h}{2}D\left(r_n + \frac{h}{2}T_n\right)\right]\right\} \\ \quad + \frac{1}{6}h\left\{T_n + hD\left[r_n + \frac{h}{2}T_n + \frac{h^2}{4}D(r_n)\right]\right\} \\ T_{n+1} = T_n + \frac{1}{6}h\left\{2D\left(r_n + \frac{h}{2}T_n\right) + 2D\left[r_n + \frac{h}{2}T_n + \frac{h^2}{4}D(r_n)\right]\right\} \\ \quad + \frac{1}{6}h\left\{D(r_n) + D\left[r_n + hT_n + \frac{h^2}{2}D(r_n)\right]\right\} \end{cases}, \tag{17}$$

where h is the step size of the ray-tracing method along the negative z axis, and D is the partial differential of n,

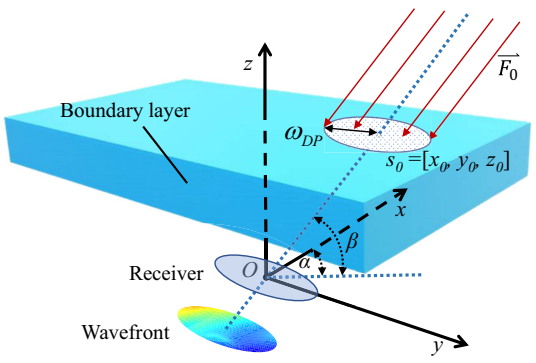

Fig. 5. Schematic diagram of photon aberrations evaluation. The photons propagate through the BL to the receiver telescope, and the wavefront aberration can be calculated by the ray-tracing method.

$$D = n\begin{pmatrix} \frac{\partial n}{\partial x} \\ \frac{\partial n}{\partial y} \\ \frac{\partial n}{\partial z} \end{pmatrix}. \tag{18}$$

The initial values s_0 and F_0 are substituted into Eq. (17) to calculate the next position s_1, and vector F_1. And then, the entire ray-tracing process can be calculated. But, to speed up the computer calculation, the values of s_0, F_0, s_1, F_1, and the refractive index field n are taken as the input parameters for the Adams linear multistep method that is combined with the interpolation method based on polynomial fitting.[45] Thus, when the Gaussian mode beam is propagating through the BL to the aircraft, the OPL of the photons can be evaluated with the ray-tracing method. Finally, the wavefront phase difference of photons can be calculated by the equation in Section 2.3.

3.2.2. Transmission efficiency

When the beam propagates through the BL and illuminates the receiving telescope, the transmission efficiency η_0 can be calculated as[44]

$$\eta_0 = \mathrm{SR} \cdot \exp\left(-\frac{\tau}{\sin\beta}\right) \cdot \left\{1 - \exp\left[-0.5\left(\frac{D_R}{\omega_{\mathrm{DP}}}\right)^2\right]\right\}, \tag{19}$$

where D_R is the diameter of the receiving telescope, and τ is the extinction optical thickness from altitude to infinity,[46] which is the reduction coefficient in brightness of stellar objects as their photons pass through the atmosphere. The effects of extinction depend on transparency, the elevation of the observer, the zenith angle, and the angle from the zenith to one's line of sight. SR is the Strehl ratio[47],

$$\mathrm{SR} \approx \exp(-\phi_{\mathrm{rms}}^2). \tag{20}$$

In the satellite-to-aircraft QKD system, the photon transmission efficiency η will be decreased, with the aero-optical effects of the aircraft BL, which can be calculated as

$$\eta = \eta_0 \eta_s \eta_d, \tag{21}$$

where η_s is the system receiving efficiency caused by constant optical components and η_d is the detector efficiency.

3.2.3. Secure key rate estimation

The decoy state is a common method in implemented experiments that combine with the QKD protocols like BB84 and measurement device independent (MDI) QKD, which can efficiently defend against the photon number splitting attacks and can perform the weak coherent photon source to replace the single-photon source in the implementations. The decoy state QKD protocol has been widely performed in fiber-based, satellite-based, and airborne-based QKD systems. Thus, in the satellite-to-aircraft QKD scheme, we perform weak-vacuum decoy BB84[48] protocol with signal photon intensity μ and decoy photon intensity ν. The modulating probability of signal (decoy) states is P_s and P_d. The final secure key rate can be calculated as

$$R \geq q\{Q_1[1 - H_2(e_1)] - Q_\mu f(E_\mu) H_2(E_\mu)\}, \tag{22}$$

where Q_1 is the gain of the received single-photon states, e_1 is the error rate of single-photon states, and $f(x)$ is the information reconciliation efficiency for correcting error bits. Q_μ and E_μ represent the gain of signal states and the overall QBER, respectively. $H_2(x)$ is the binary Shannon entropy, which can be calculated as

$$H_2(x) = -x\log(x) - (1-x)\log(1-x). \tag{23}$$

Given the photon transmission efficiency η, Q_μ is calculated as

$$Q_\mu = Y_0 + 1 - e^{-\eta\mu}, \tag{24}$$

where Y_0 is the dark count rate of QKD systems. Thus, the error gain of signal quantum states can be given by

$$E_\mu Q_\mu = e_0 Y_0 + e_d(1 - e^{-\eta\mu}), \tag{25}$$

where e_0 is the error rate of dark counts, usually $e_0 = 0.50$. e_d is the misalignment error rate of QKD systems.

Thus, the QBER E_μ can be calculated as

$$E_\mu = E_\mu Q_\mu / Q_\mu. \tag{26}$$

The gain of single-photon states Q_1 can be calculated as

$$Q_1 \geq Q_1^{L,\nu,0} = \frac{\mu^2 e^{-\mu}}{\mu\nu - \nu^2}\left(Q_\nu e^\nu - Q_\mu e^\mu \frac{\nu^2}{\mu^2} - \frac{\mu^2 - \nu^2}{\mu^2} Y_0\right), \tag{27}$$

where L denotes the lower bound value, and Q_ν is the gain of decoy states.

The error rate of single-photon states e_1 can be calculated as

$$e_1 \leq e_1^{U,\nu,0} = \frac{E_\nu Q_\nu e^\nu - e_0 Y_0}{Y_1^{L,\nu,0}\nu}, \tag{28}$$

where $Y_1^{L,\nu,0}$ is the yield of single-photon states,

$$Y_1^{L,\nu,0} = \frac{Q_1}{\mu e^{-\mu}}. \tag{29}$$

The error gain of decoy states $E_\nu Q_\nu$ can be calculated as

$$E_\nu Q_\nu = e_0 Y_0 + e_d(1 - e^{-\eta\nu}). \tag{30}$$

Afterward, the QBER E_μ and secure key rate R can be obtained by taking the photon transmission efficiency η into weak-vacuum decoy BB84 protocol.

4. Performance Analysis

The specific parameters of the aircraft, quantum photon source payload, and optical receiving module are shown in Table 1. Some parameters refer to the Micius quantum experiment science satellite in the literature[10].

Here, the typical wing-body configuration DLR-F6 is chosen for the performance analysis of our specified satellite-to-aircraft QKD system. Given the detailed aircraft description from Table 1, the BL will be generated around the DLR-F6[49] and its density field distribution can be simulated by the computational fluid dynamics software (Ansys Fluent), as shown in Fig. 6. Assuming that the receiver telescope that conforms with the aircraft is fixed in the symmetry axis of the upper fuselage surface, the 500 mm × 500 mm × 50 mm BL above the fuselage has been taken, as shown in Fig. 6. Afterward, the refractive index distribution can be calculated by Eq. (5). For convenience, the projecting distances between the geometric center of the receiver telescope and the tip of the nose in the flight direction are denoted as X_0. The value of X_0 should be greater than 37 mm to avoid the flight deck, which is temporarily set as 66 mm.

Table 1. Parameters of Airborne QKD.

Payload	Parm.	Description	Value
Aircraft	v	Flight speed	0.7 Ma
	h_B	Altitude of aircraft	10 km
	ρ_h	Air density	0.413 kg/m^3
	τ	Extinction optical thickness[46]	0.02
Photon source	D_T	Diameter of the transmitter telescope	0.3 m
	δ_T	Transmitter pointing precision[10]	10 μrad
	λ	Transmitter wavelength	1550 nm
	ω_0	Waist radius	0.0949 m
	r_0	Fried parameter in zenith[44]	0.4 m
	μ	Intensity of signal states	0.8
	ν	Intensity of decoy states	0.1
	N	System repetition rate	100 MHz
	P_s	Probability of signal states	50%
	P_d	Probability of decoy states	30%
	P_v	Probability of vacuum states	25%
Receiving module	D_R	Diameter of the receiver telescope	0.5 m
	e_d	System detection error rate	1%
	p_d	Dark count rate	2×10^{-6}
	η_d	Detector efficiency	50%
	η_s	Receiving optical module efficiency	60%

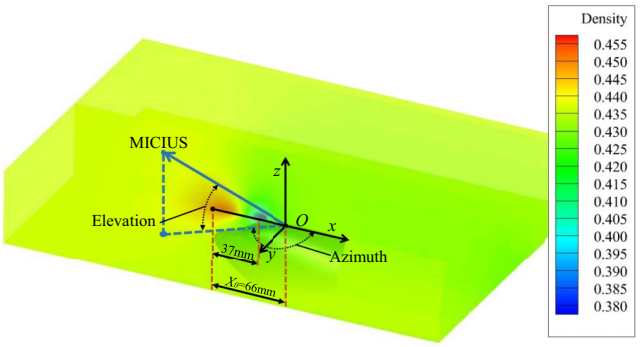

Fig. 6. Evaluated density field distribution of the DLR-F6 BL. The dimensions of the BL are 500 mm × 500 mm × 50 mm.

In the coordinate system shown in Fig. 6, assume that the satellite orbits the earth at an altitude of 500 km that is directly over the aircraft at various azimuths. Setting azimuth angle α = 0°, 90°, 180°, 270° and elevation angle $10^\circ \le \beta \le 90^\circ$, the total loss at different incident angles can be calculated as shown in Fig. 7. As the elevation angle increases, the total loss declines sharply, which indicates that the loss is generally high when the elevation angle $\beta \le 30^\circ$. Moreover, when $\alpha = 180^\circ$ and $30^\circ \le \beta \le 90^\circ$, the total loss also increases on average about 3 dB. This indicates that when the aircraft moves toward the satellite, the effects of the BL are more serious. So, to reduce the influence of the BL, with permission to adjust the direction of flight, it is possible to change the direction of flight and turn the aircraft away from the satellite.

Assume that the aircraft is flying at a constant speed $v = 0.7$ Ma, altitude $h_B = 10$ km, and heads due south or east, and the initial position of aircraft is (34°15′56″N, 108°57′13″E). It is assumed that the aircraft returns to the initial position after each orbit of communication is completed. We import the satellite ephemeris of Micius and the aircraft trajectory into

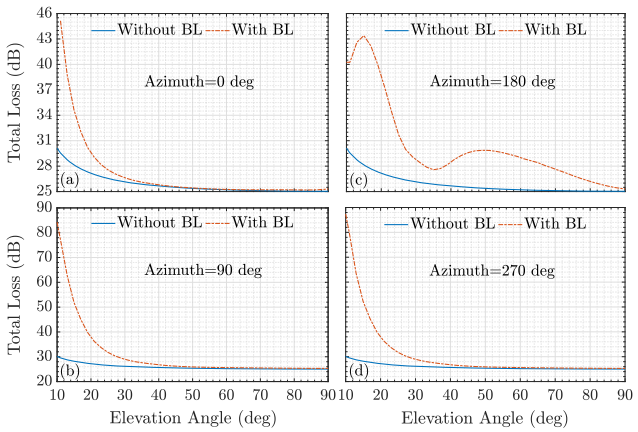

Fig. 7. Total loss over the different incident angles. Here they are α = 0°, 90°, 180°, 270°.

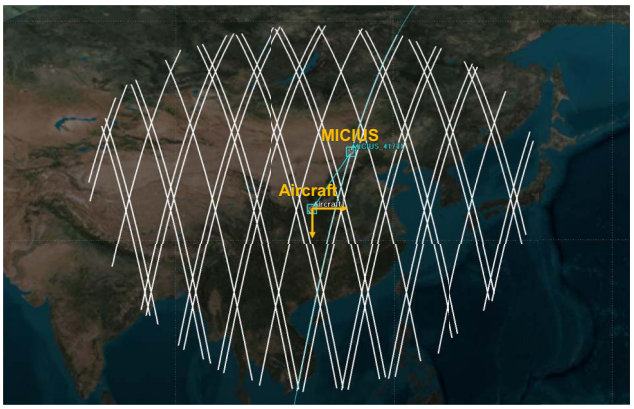

Fig. 8. Schematic diagram of satellite-to-aircraft QKD from 12:00 on May 29, 2022, to 12:00 on June 5, 2022. The yellow arrow indicates the direction of flight of the aircraft.

the Satellite Tool Kit (STK) from 12:00 on May 29, 2022, to 12:00 on June 5, 2022. The schematic diagram of satellite-to-aircraft QKD is shown in Fig. 8; all the trajectories of Micius that establish available communication links of satellite-to-aircraft QKD are marked.

Then, during a week, the performance of the whole satellite-to-aircraft QKD session is evaluated. When the aircraft is heading south, the result is shown in Fig. 9. Significantly, the abscissa represents the link time of all established links in a week, and the total link time is 6800 s. The additional channel loss to the transmitted photons is around 30 dB during the total link time, as shown in Fig. 9(a). The time when the secure key rate is more than zero is denoted as the quantum communication time. Therefore, the total quantum communication time is 3625 s, as shown in Fig. 9(c), and the estimated total final key size is around 6.718×10^6 bits. When the aircraft is heading east, the result is shown in Fig. 10. The additional channel loss to the transmitted photons is around 32 dB during the total link time, as shown in Fig. 10(a). The total quantum communication time

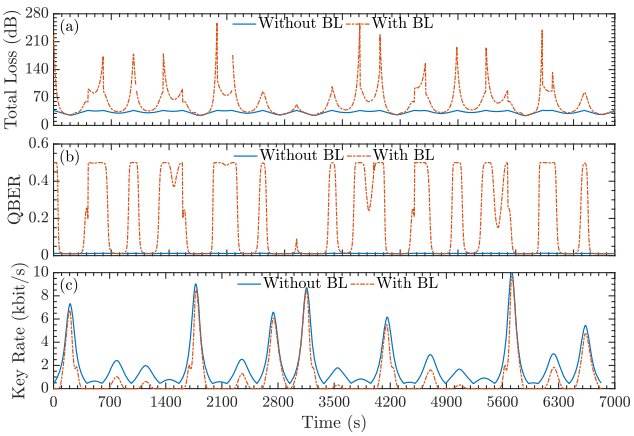

Fig. 9. (a) Total loss in the satellite-to-aircraft QKD scenario; (b) estimated QBER over the communication time; (c) secure key rate over the communication time. The value of X_0 is 66 mm and the aircraft flights toward the south. The intensity of signal states is 0.8, and the intensity of decoy states is 0.1.

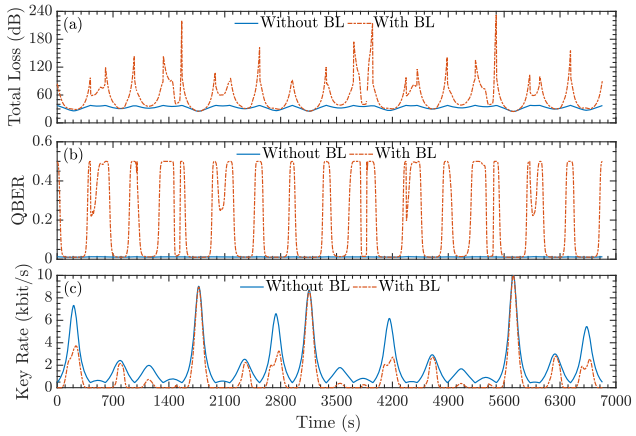

Fig. 10. (a) Total loss in the satellite-to-aircraft QKD scenario; (b) estimated QBER over the communication time; (c) secure key rate over the communication time. The value of X_0 is 66 mm and the aircraft flights toward the east. The intensity of signal states is 0.8, and the intensity of decoy states is 0.1.

is 3685 s, as shown in Fig. 10(c), and the estimated total final key size is around 6.322×10^6 bits. If there is no BL surrounding the aircraft, the estimated secure key rate would be around 1.326×10^7 bits. In summary, the BL effects cannot be ignored in the satellite-to-aircraft QKD scenario and heavily decrease the final secure key rate.

5. Conclusion

Airborne QKD will be a flexible bond between the terrestrial fiber QKD network and quantum satellites, which can establish a mobile, on-demand, and real-time coverage quantum network. However, the randomly distributed BL always surrounds the surface of the aircraft, which would introduce random wavefront aberration, jitter, and extra intensity attenuation to the transmitted photons between the aircraft and the ground station. Previous research of airborne QKD with BL effects is mainly under the air-to-ground scenario, while the satellite-to-aircraft scenario is rarely reported. In this article, we proposed a detailed performance evaluation scheme of satellite-to-aircraft QKD with BL effects. The analyzed photon transmission loss shows that the effects of the BL are more serious when the aircraft moves towards the satellite. In our proposed satellite-to-aircraft QKD scenario, the BL would introduce ~31 dB loss to the transmitted photons, decrease ~47% of the quantum communication time, and decrease ~51% of the secure key rate. This indicates that the aero-optical effects caused by the BL cannot be ignored. Our detailed satellite-to-aircraft QKD performance evaluation study can be used in future airborne quantum communication designs.

Acknowledgement

This work is supported by the National Natural Science Foundation of China (Nos. 61971436, 61972410, and

61803382), the Natural Science Basic Research Plan in Shaanxi Province of China (No. 2018020JQ6020), the Research Plan of National University of Defense Technology (Nos. ZK19-13 and 19-QNCXJ-107), and the Postgraduate Scientific Research Innovation Project of Hunan Province (No. CX20200003).

References

1. I. M. Arbekov and S. N. Molotkov, "Secret keys agreement in communication networks with quantum key distribution and trusted nodes," Laser Phys. Lett. **17**, 055202 (2020).
2. C. Erven, B. Heim, E. Meyer-Scott, J. P. Bourgoin, R. Laflamme, G. Weihs, and T. Jennewein, "Studying free-space transmission statistics and improving free-space quantum key distribution in the turbulent atmosphere," New J. Phys. **14**, 123018 (2012).
3. E. Kaur, M. M. Wilde, and A. Winter, "Fundamental limits on key rates in device-independent quantum key distribution," New J. Phys. **22**, 023039 (2020).
4. N. Lütkenhaus and A. J. Shields, "Focus on quantum cryptography: theory and practice," New J. Phys. **11**, 045005 (2009).
5. D. Stucki, M. Legré, F. Buntschu, B. Clausen, N. Felber, N. Gisin, L. Henzen, P. Junod, G. Litzistorf, P. Monbaron, L. Monat, J.-B. Page, D. Perroud, G. Ribordy, A. Rochas, S. Robyr, J. Tavares, R. Thew, P. Trinkler, S. Ventura, R. Voirol, N. Walenta, and H. Zbinden, "Long-term performance of the SwissQuantum quantum key distribution network in a field environment," New J. Phys. **13**, 123001 (2011).
6. W. Chen, Z. Han, T. Zhang, H. Wen, Z. Yin, F. Xu, Q. Wu, Y. Liu, Y. Zhang, X. Mo, Y. Gui, G. Wei, and G. Guo, "Field experiment on a "star type" metropolitan quantum key distribution network," IEEE Photon. Technol. Lett. **21**, 575 (2009).
7. S. Wang, W. Chen, Z.-Q. Yin, D.-Y. He, C. Hui, P.-L. Hao, G.-J. Fan-Yuan, C. Wang, L.-J. Zhang, J. Kuang, S.-F. Liu, Z. Zhou, Y.-G. Wang, G.-C. Guo, and Z.-F. Han, "Practical gigahertz quantum key distribution robust against channel disturbance," Opt. Lett. **43**, 2030 (2018).
8. X.-B. Wang, Z.-W. Yu, and X.-L. Hu, "Twin-field quantum key distribution with large misalignment error," Phys. Rev. A **98**, 062323 (2018).
9. W. Kozlowski and S. Wehner, "Towards large-scale quantum networks," in *Proceedings of the Sixth Annual ACM International Conference on Nanoscale Computing and Communication* (Association for Computing Machinery, 2019), p. 3.
10. S.-K. Liao, W.-Q. Cai, W.-Y. Liu, L. Zhang, Y. Li, J.-G. Ren, J. Yin, Q. Shen, Y. Cao, Z.-P. Li, F.-Z. Li, X.-W. Chen, L.-H. Sun, J.-J. Jia, J.-C. Wu, X.-J. Jiang, J.-F. Wang, Y.-M. Huang, Q. Wang, Y.-L. Zhou, L. Deng, T. Xi, L. Ma, T. Hu, Q. Zhang, Y.-A. Chen, N.-L. Liu, X.-B. Wang, Z.-C. Zhu, C.-Y. Lu, R. Shu, C.-Z. Peng, J.-Y. Wang, and J.-W. Pan, "Satellite-to-ground quantum key distribution," Nature **549**, 43 (2017).
11. L. Calderaro, C. Agnesi, D. Dequal, F. Vedovato, M. Schiavon, A. Santamato, V. Luceri, G. Bianco, G. Vallone, and P. Villoresi, "Towards quantum communication from global navigation satellite system," Quantum Sci. Technol. **4**, 015012 (2018).
12. S.-K. Liao, H.-L. Yong, C. Liu, G.-L. Shentu, D.-D. Li, J. Lin, H. Dai, S.-Q. Zhao, B. Li, J.-Y. Guan, W. Chen, Y.-H. Gong, Y. Li, Z.-H. Lin, G.-S. Pan, J. S. Pelc, M. M. Fejer, W.-Z. Zhang, W.-Y. Liu, J. Yin, J.-G. Ren, X.-B. Wang, Q. Zhang, C.-Z. Peng, and J.-W. Pan, "Long-distance free-space quantum key distribution in daylight towards inter-satellite communication," Nat. Photonics **11**, 509 (2017).
13. J. Yin, Y. Cao, Y.-H. Li, J.-G. Ren, S.-K. Liao, L. Zhang, W.-Q. Cai, W.-Y. Liu, B. Li, H. Dai, M. Li, Y.-M. Huang, L. Deng, L. Li, Q. Zhang, N.-L. Liu, Y.-A. Chen, C.-Y. Lu, R. Shu, C.-Z. Peng, J.-Y. Wang, and J.-W. Pan, "Satellite-to-ground entanglement-based quantum key distribution," Phys. Rev. Lett. **119**, 200501 (2017).
14. J. Yin, Y.-H. Li, S.-K. Liao, M. Yang, Y. Cao, L. Zhang, J.-G. Ren, W.-Q. Cai, W.-Y. Liu, S.-L. Li, R. Shu, Y.-M. Huang, L. Deng, L. Li, Q. Zhang, N.-L. Liu, Y.-A. Chen, C.-Y. Lu, X.-B. Wang, F. Xu, J.-Y. Wang, C.-Z. Peng, A. K. Ekert, and J.-W. Pan, "Entanglement-based secure quantum cryptography over 1,120 kilometres," Nature **582**, 501 (2020).
15. S.-K. Liao, W.-Q. Cai, J. Handsteiner, B. Liu, J. Yin, L. Zhang, D. Rauch, M. Fink, J.-G. Ren, W.-Y. Liu, Y. Li, Q. Shen, Y. Cao, F.-Z. Li, J.-F. Wang, Y.-M. Huang, L. Deng, T. Xi, L. Ma, T. Hu, L. Li, N.-L. Liu, F. Koidl, P. Wang, Y.-A. Chen, X.-B. Wang, M. Steindorfer, G. Kirchner, C.-Y. Lu, R. Shu, R. Ursin, T. Scheidl, C.-Z. Peng, J.-Y. Wang, A. Zeilinger, and J.-W. Pan, "Satellite-relayed intercontinental quantum network," Phys. Rev. Lett. **120**, 030501 (2018).
16. Y.-A. Chen, Q. Zhang, T.-Y. Chen, W.-Q. Cai, S.-K. Liao, J. Zhang, K. Chen, J. Yin, J.-G. Ren, Z. Chen, S.-L. Han, Q. Yu, K. Liang, F. Zhou, X. Yuan, M.-S. Zhao, T.-Y. Wang, X. Jiang, L. Zhang, W.-Y. Liu, Y. Li, Q. Shen, Y. Cao, C.-Y. Lu, R. Shu, J.-Y. Wang, L. Li, N.-L. Liu, F. Xu, X.-B. Wang, C.-Z. Peng, and J.-W. Pan, "An integrated space-to-ground quantum communication network over 4,600 kilometres," Nature **589**, 214 (2021).
17. Y. Xue, W. Chen, S. Wang, Z. Yin, L. Shi, and Z. Han, "Airborne quantum key distribution: a review [Invited]," Chin. Opt. Lett. **19**, 122702 (2021).
18. C.-Y. Lu, Y. Cao, C.-Z. Peng, and J.-W. Pan, "Micius quantum experiments in space," Rev. Mod. Phys. **94**, 035001 (2022).
19. S. Nauerth, F. Moll, M. Rau, C. Fuchs, J. Horwath, S. Frick, and H. Weinfurter, "Air-to-ground quantum communication," Nat. Photonics **7**, 382 (2013).
20. H.-Y. Liu, X.-H. Tian, C. Gu, P. Fan, X. Ni, R. Yang, J.-N. Zhang, M. Hu, J. Guo, X. Cao, X. Hu, G. Zhao, Y.-Q. Lu, Y.-X. Gong, Z. Xie, and S.-N. Zhu, "Optical-relayed entanglement distribution using drones as mobile nodes," Phys. Rev. Lett. **126**, 020503 (2021).
21. C. J. Pugh, S. Kaiser, J.-P. Bourgoin, J. Jin, N. Sultana, S. Agne, E. Anisimova, V. Makarov, E. Choi, B. L. Higgins, and T. Jennewein, "Airborne demonstration of a quantum key distribution receiver payload," Quantum Sci. Technol. **2**, 024009 (2017).
22. A. DeCesare, R. Snyder, D. Carvalho, W. Miller, P. Alsing, and D. Ahn, "Toward mobile free-space optical QKD: characterization of a polarization-based receiver," Proc. SPIE **11391**, 1139105 (2020).
23. H. Liu, X.-H. Tian, C. Gu, P. Fan, X. Ni, R. Yang, J.-N. Zhang, M. Hu, J. Guo, X. Cao, X. Hu, G. Zhao, Y.-Q. Lu, Y.-X. Gong, Z. Xie, and S.-N. Zhu, "Drone-based entanglement distribution towards mobile quantum networks," Natl. Sci. Rev. **7**, 921 (2020).
24. M. Zhang, L. Zhang, J. Wu, S. Yang, X. Wan, Z. He, J. Jia, D. S. Citrin, and J. Wang, "Detection and compensation of basis deviation in satellite-to-ground quantum communications," Opt. Express **22**, 9871 (2014).
25. F. Moll, T. Botter, C. Marquardt, D. Pusey, A. Shrestha, A. Reeves, K. Jaksch, K. Gunthner, O. Bayraktar, C. Mueller-Hirschkorn, A. D. Gallardo, D. Diaz Gonzalez, W. Rosenfeld, P. Freiwang, G. Leuchs, and H. Weinfurter, "Stratospheric QKD: feasibility analysis and free-space optics system concept," Proc. SPIE **11167**, 111670H (2019).
26. X. Yan, P.-F. Zhang, J.-H. Zhang, C.-H. Qiao, and C.-Y. Fan, "Quantum polarization fluctuations of partially coherent dark hollow beams in non-Kolmogorov turbulence atmosphere," Chin. Phys. B **25**, 084204 (2016).
27. C. Bonato, M. Aspelmeyer, T. Jennewein, C. Pernechele, P. Villoresi, and A. Zeilinger, "Influence of satellite motion on polarization qubits in a Space-Earth quantum communication link," Opt. Express **14**, 10050 (2006).
28. M. Toyoshima, H. Takenaka, and Y. Takayama, "Atmospheric turbulence-induced fading channel model for space-to-ground laser communications links," Opt. Express **19**, 15965 (2011).
29. G. A. Tyler and R. W. Boyd, "Influence of atmospheric turbulence on the propagation of quantum states of light carrying orbital angular momentum," Opt. Lett. **34**, 142 (2009).
30. A. V. Anufriev, Y. A. Zimin, A. L. Vol'pov, and I. N. Matveev, "Change in the polarization of light in a turbulent atmosphere," Sov. J. Quantum Electron. **13**, 1627 (1983).
31. X. Shan, X. Sun, J. Luo, Z. Tan, and M. Zhan, "Free-space quantum key distribution with Rb vapor filters," Appl. Phys. Lett. **89**, 191121 (2006).
32. J. Yin, J.-G. Ren, H. Lu, Y. Cao, H.-L. Yong, Y.-P. Wu, C. Liu, S.-K. Liao, F. Zhou, Y. Jiang, X.-D. Cai, P. Xu, G.-S. Pan, J.-J. Jia, Y.-M. Huang, H. Yin, J.-Y. Wang, Y.-A. Chen, C.-Z. Peng, and J.-W. Pan, "Quantum teleportation and entanglement distribution over 100-kilometre free-space channels," Nature **488**, 185 (2012).
33. W. T. Buttler, R. J. Hughes, S. K. Lamoreaux, G. L. Morgan, J. E. Nordholt, and C. G. Peterson, "Daylight quantum key distribution over 1.6 km," Phys. Rev. Lett. **84**, 5652 (2000).

34. S. Gordeyev, A. E. Smith, J. A. Cress, and E. J. Jumper, "Experimental studies of aero-optical properties of subsonic turbulent boundary layers," J. Fluid Mech. **740**, 214 (2014).
35. S. Gordeyev, M. R. Rennie, A. B. Cain, and T. Hayden, "Aero-optical measurements of high-Mach supersonic boundary layers," in *46th AIAA Plasmadynamics and Lasers Conference* (2015), p. 3246.
36. H.-C. Yu, B.-Y. Tang, H. Chen, Y. Xue, J. Tang, W.-R. Yu, B. Liu, and L. Shi, "Airborne quantum key distribution with boundary layer effects," EPJ Quantum Technol. **8**, 26 (2021).
37. W. Merzkirch, "3-optical flow visualization," in *Flow Visualization*, 2nd ed., W. Merzkirch, ed. (Academic Press, 1987), p. 115.
38. X. Ren, J. Wang, G. Ren, J. Zhai, Y. Tan, and X. Yang, "Solving the differential equation of light rays in Cartesian coordinates," Optik **194**, 163055 (2019).
39. M. Jones and E. Bender, "CFD-based computer simulation of optical turbulence through aircraft flowfields and wakes," in *32nd AIAA Plasmadynamics and Lasers Conference* (American Institute of Aeronautics and Astronautics, 2001).
40. G. Guo, H. Liu, and B. Zhang, "Aero-optical effects of an optical seeker with a supersonic jet for hypersonic vehicles in near space," Appl. Opt. **55**, 4741 (2016).
41. X.-W. Sun, X.-L. Yang, and W. Liu, "Aero-optical suppression for supersonic turbulent boundary layer," J. Turbul. **22**, 1 (2021).
42. H. Ding, S. Yi, X. Zhao, J. Yi, and L. He, "Research on aero-optical prediction of supersonic turbulent boundary layer based on aero-optical linking equation," Opt. Express **26**, 31317 (2018).
43. H. Ding, S. Yi, Y. Zhu, and L. He, "Experimental investigation on aero-optics of supersonic turbulent boundary layers," Appl. Opt. **56**, 7604 (2017).
44. S. P. Neumann, S. K. Joshi, M. Fink, T. Scheidl, R. Blach, C. Scharlemann, S. Abouagaga, D. Bambery, E. Kerstel, M. Barthelemy, and R. Ursin, "Q3Sat: quantum communications uplink to a 3U CubeSat—feasibility & design," EPJ Quantum Technol. **5**, 4 (2018).
45. H. Xiong, S. Yi, H. Ding, X. Xu, and T. Ouyang, "New ray tracing method for 3D irregular non-uniform refractive index field," Infrared Laser Eng. **48**, 503005 (2019).
46. L. Elterman, *UV, Visible, and IR Attenuation for Altitudes to 50 km* (Air Force Cambridge Research Laboratories, Office of Aerospace Research, United States Air Force, 1968).
47. T. S. Ross, "Limitations and applicability of the Maréchal approximation," Appl. Opt. **48**, 1812 (2009).
48. X. Ma, B. Qi, Y. Zhao, and H.-K. Lo, "Practical decoy state for quantum key distribution," Phys. Rev. A **72**, 012326 (2005).
49. O. Brodersen and A. Stuermer, "Drag prediction of engine-airframe interference effects using unstructured Navier-Stokes calculations," in *19th AIAA Applied Aerodynamics Conference* (American Institute of Aeronautics and Astronautics, 2001).